Chemical Engineering Journal 499 (2024) 155718

Contents lists available at ScienceDirect

Chemical Engineering Journal

journal homepage: www.elsevier.com/locate/cej

Model-driven design and validation of glucose supply control in a tubular photobioreactor operated under oxygen-balanced mixotrophy

Pedro Moñino Fernández [1], Luca Buscaglia [1], Daan Jordaan, Maria Barbosa, Marcel Janssen *

Bioprocess Engineering, AlgaePARC, Wageningen University and Research, P.O. Box 16, 6700 AA Wageningen, the Netherlands

ARTICLE INFO

Keywords:
Oxygen-balanced mixotrophy
PID controller
Tank-in-series model
Tubular photobioreactor
Scale-down validation

ABSTRACT

Scaling up bioprocesses remains challenging due to the partially unpredictable and suboptimal behavior of microbes during scale transition. Mathematical modelling serves as a valuable tool in navigating these challenges. In this study, we developed and validated a kinetic model based on the tank-in-series approach for a novel bioprocess known as oxygen-balanced mixotrophy with the microalga *Galdieria sulphuraria*. This model aims to facilitate the design of an effective glucose feeding control strategy tailored for two-phase tubular photobioreactors (*TPBRs*). The residence time distribution of our reference reactor was investigated by means of a tracer experiment. Qualitative analysis of the results indicated that our system was optimally represented by simulations with a 100 stirred-tank reactors (*STRs*).

The controlled variable, oxygen concentration in the gas phase, showed a downward trend in simulations with simplified conditions: fixed oxygen production and balanced glucose supply. The decrease was caused by dominant net heterotrophic activity and accumulation of CO_2 in the gas phase. Different configurations of a proportional-integral-derivative (*PID*) controller were designed by means of the ultimate gain method and compared under these simplified conditions. The most effective *PID* controller was implemented and refined in simulations with outdoor weather conditions. The model was validated successfully by simulating over time in a lab-scale *STR* the spatial fluctuations happening in a *TPBR*. The empirical oxygen consumption and production were faster and steeper than in the model, probably due to inaccuracies in parameter estimation or biomass adaptation.

1. Introduction

The bioeconomy has emerged as a path for sustainable development that shifts away from conventional fossil fuel industry [1]. In this sense, there is a growing demand for large-scale bioprocesses that can economically meet the diverse needs of various markets [2]. However, transitioning from lab-scale developments to industrial-scale production has encountered several challenges, primarily due to the loss of product yield and productivity during scale-up [3,4]. These unwanted effects are a consequence of the complex interplay of physical, chemical and biological phenomena inherent to bioprocesses and have yet to be fully untangled. One effective strategy to bridge this gap comes from the development of computer-aided mathematical models [5]. The integration of these models can significantly enhance the scale-up design, automation and control of biotechnological processes, aligning the field more closely to the well-established practices in chemical engineering.

Microalgal bioprocesses have received special attention due to lack of arable land requirements, high areal productivities in comparison to traditional plant crops and rich biomass composition [6]. Despite these interesting features, modelling autotrophic processes introduces an additional layer of complexity compared to heterotrophic cultivation due to cell interaction with light and other environmental factors [7]. Although numerous approaches have been proposed to address these challenges, applications for advanced scale-up tasks remain limited. Most control efforts have focused on pH regulation by CO_2 injection to improve CO_2 uptake efficiency [8,9,10]. Some studies have also focused on controlling biomass concentration to optimize productivity [11].

Recently, we have developed a new type of microalgal process denominated oxygen-balanced mixotrophy (*OBM*) using the polyextremophilic species *Galdieria sulphuraria* [12,13]. *OBM* combines autotrophic and heterotrophic growth in a balanced manner through careful regulation of the organic carbon substrate supply. This

* Corresponding author.
E-mail addresses: pedro.moninofernandez@wur.nl (P. Moñino Fernández), marcel.janssen@wur.nl (M. Janssen).
[1] Authors contributed equally.

https://doi.org/10.1016/j.cej.2024.155718
Received 12 April 2024; Received in revised form 7 September 2024; Accepted 10 September 2024
Available online 13 September 2024

adjustment ensures the stability of dissolved oxygen (*DO*) in the medium by harmonizing heterotrophic oxygen consumption and photosynthetic oxygen production, which results in intracellular gas recycling. The advantages of this novel process include the possibility of running a reactor without any gas exchange during daylight hours, achieving a high biomass yield on substrate and improve autotrophic productivity.

OBM was initially developed in a lab-scale stirred-tank reactor (*STR*), where the control of substrate supply is relatively straightforward, as the system resembles an ideally mixed vessel [14]. On the contrary, substrate feeding in large-scale photobioreactors is more challenging due to the different mixing patterns associated to volume scale-up. For example, the most common closed reactor configuration for large-scale microalgae cultivation are tubular photobioreactors (*TPBRs*), characterized by plug flow behavior [15]. Fluctuations in substrate or other critical compounds such as O_2 lead to suboptimal process performance and affect the biomass adversely [16]. A well-designed control strategy is essential, considering that extensive trial-and-error empirical optimization at large scale is time-consuming and prone to failure.

To address this challenge, we propose a novel computational approach for designing the control of glucose supply in a *TPBR*. Initially, we developed a kinetic model of the reactor, using as a reference a *TPBR* from our pilot facility AlgaePARC. This *TPBR* is characterized by a two-phase wavy-flow in the tubular section without a typical degasser vessel. The model was based on the simulation of a series of co-current *STRs* that mimic plug flow behavior. Subsequently, we used this model to design and optimize a control strategy for glucose supply that followed the concentration of O_2 in the gas phase. This strategy was based on a proportional-integral-derivative control algorithm. Finally, the model and the control *in silico* were validated in a lab setting by scaling down the *TPBR*. Our approach was based on the equivalences between a batch process and a plug flow reactor.

2. Materials and methods

2.1. Model approach

A mathematical model was developed to describe the behavior of oxygen-balanced mixotrophy (*OBM)* in a tubular photobioreactor (*TPBR)* using the strain *G. sulphuraria* ACUF 064. The primary goal was to design the glucose supply strategy at pilot scale. The model was constructed based on the plug flow behavior that characterizes the tubular section of *TPBRs* (i.e. the solar collector). These fluid dynamics were approximated by a series of ideal stirred-tank reactors (*STRs*), commonly referred as the tank-in-series (*TIS*) model [17]. This modelling approach leads to equivalent results as the plug flow dispersion model (in case of small deviations from plug flow) and presents a number of advantages. It is simpler to use, more straightforward to interpret, and can be easily extended for the multiphase flows with recycle such as the one presented in this study. Furthermore, this model accounts for the typical delay between the inlet and outlet that is characteristic of tubular systems, which was measured during the pulse experiments, described in section 2.3. Pulse input experiment. The delay implies that a disturbance originating in the tubular section of the photobioreactor can only be measured when it reaches the position of the appropriate sensor, after propagating in the tubes. This phenomenon significantly impacts the selection of the process control strategy, highlighting the importance of strategies optimized for time-delay systems. Another crucial aspect is that model simulations focused on a single daytime period. After sunset, *OBM* becomes infeasible and aeration is required. Aeration resets the conditions to the same "initial" state each night. The length of the simulated daytime was based on Dutch summer, ranging from 14.5 to 16 h depending on the specific simulation. Throughout these simulations, temperature and pressure were assumed to be constant at 37 °C and standard atmospheric pressure, respectively.

2.2. Flow configuration and dimensions of the simulated TPBR

The dimensions and flowrate configuration of the modelled *TPBR* were based on the GemTube MK-1 1500 s *TPBR* (Lgem, the Netherlands) located in AlgaePARC, our greenhouse pilot facility (Bennekom, the Netherlands) (Fig. 1). The system consisted of two symmetrical helicoidal tubes of 280-m length with internal diameter of 6.2 cm. Both helices are connected to a collection vessel which can be considered a dark volume. We assumed that both helices behave similarly and thus only one helix was simulated. Moreover, biomass loss in the collection vessel was neglected as its working volume (50 L) is considerably lower than the total liquid working volume (1300 L). Mass transfer in the collection vessel was also neglected as the liquid inside was not sparged. Instead, gas is injected directly into the tubes at the lowest part of the helix, which creates a two-phase flow with an elongated bubble regime that leads to oxygen (O_2) and carbon dioxide (CO_2) mass transfer along the tubular section. This aspect was taken into account in the model by simulating co-current gas and liquid phases in every hypothetical *STR*. As in *OBM* there is no external gas input, the gas phase at the end of the tube is recycled and serves as input for the first *STR*. In addition, we neglected the concentration gradients in the gas and the liquid phase in the radial direction of the tube and ideal behavior of the gas phase.

2.3. Pulse input experiment

The residence-time distribution (*RTD*) of the reference *TPBR* was analyzed by means of a pulse input experiment with HCl as a tracer. The pulse was manually supplied to the reactor by pouring 500 mL of acid from a bottle into the collection vessel. The evolution of pH was then monitored by a pH probe located between the collection vessel and the split of the reactor helices (Fig. 1). Measurements were taken every 2 s and the data was logged every minute as the average of the previous 30 measurements. In total, three runs were performed on different days, one with 1 M HCl and two runs with 2 M of HCl. During the runs the *TPBR* was operated with a gas flowrate (F_G) of 20 L min^{-1} and a liquid flowrate (F_L) of 53 L min^{-1} in the helix. Only the first passage of the tracer pulse was considered for the determination of the *RTD*. Initially, the pH signal was converted into proton concentration as a function of time, *C(t)*. The *RTD* function *E(t)* was then subsequently derived as follows:

$$E(t) = \frac{C(t)}{\int_0^\infty C(t)dt}. \quad (1)$$

2.4. Autotrophic oxygen production

The biomass concentration (C_x, C-$mol_x \cdot m^{-3}$) was assumed constant during the simulated daytime period with the aim of simplifying model construction. Because of the short time frame simulated, neglecting biomass increase does not incur a large error. In addition, the volumetric biomass productivity (r_x, C-$mol_x \cdot m^{-3} \cdot s^{-1}$) remains constant when C_x stays within an optimal range under light limited conditions [12]. r_x is the product of C_x and the specific growth rate (μ, s^{-1}). An increase in C_x is thus balanced by an equivalent decrease in μ leading to a constant r_x. This implies that the volumetric production and consumption rates of O_2 and CO_2 are also constant. In this sense, a fixed C_x represents the average concentration during the simulated time frame. Such C_x and its associated autotrophic average specific oxygen production ($q_{O,auto}$, $mol_{O2} \cdot C\text{-}mol_x^{-1} \cdot s^{-1}$) were estimated from previous empirical data obtained in a lab-scale *STR* operated in chemostat with excess CO_2 and a volumetric light supply rate comparable with what it could be expected in a large-scale *TPBR* [13] (Table 1). Thus, $q_{O,auto}$ represents the maximum specific autotrophic oxygen production rate in the model conditions with constant light.

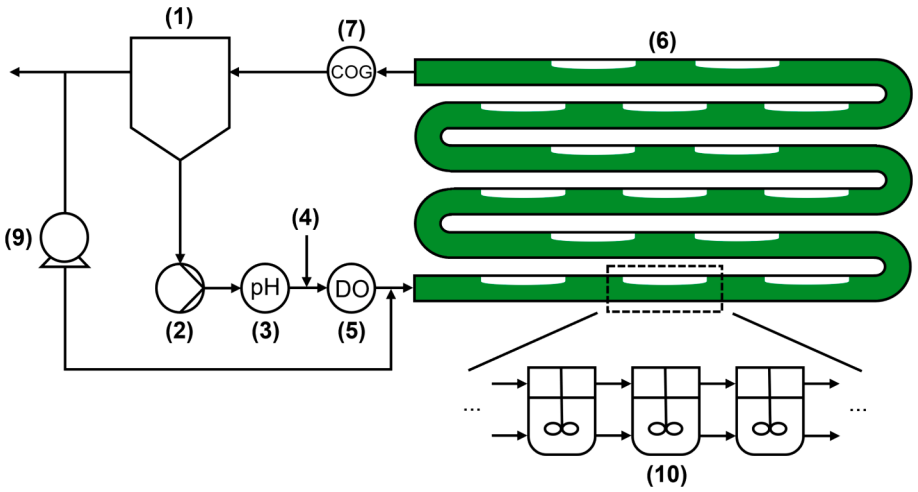

Fig. 1. Schematic representation of the reference tubular photobioreactor and the tank-in-series model. The configuration of the reactor is adapted to the tracer experiment and the oxygen-balanced mixotrophic operation described in the model. The numbers indicate different parts of the system: (1) collection vessel, (2) liquid recirculation pump, (3) pH probe, (4) glucose injection point, (5) dissolved oxygen probe, (6) tubular section, (7) oxygen in the gas probe, (8) bleed gas, (9) gas compressor and (10) series of ideal stirred-tank reactors. The dissolved oxygen sensor is placed in the most critical location of the process, right after the substrate injection point and just before the section at the highest mass transfer rate.

Table 1
Operational, biological and physical parameters used in the model by order of appearance.

Parameter	Value	Unit	Reference
C_x	4.5	$g{\cdot}L^{-1}$	[13]
$q_{O,auto}$	$1.96{\cdot}10^{-6}$	$mol_{O2}{\cdot}C\text{-}mol_x^{-1}{\cdot}s^{-1}$	[13]
$Y_{x/s}$	0.59	$C\text{-}mol_x{\cdot}C\text{-}mol_s^{-1}$	[12]
F_L^{in}	$8.78{\cdot}10^{-4}$	$m^3{\cdot}s^{-1}$	This study
V_L	0.61	m^3	This study
C_{sFEED}	200	$g{\cdot}L^{-1}$	This study
q_{smax}	$1.15{\cdot}10^{-5}$	$C\text{-}mol_s{\cdot}C\text{-}mol_x^{-1}{\cdot}s^{-1}$	This study
K_s	$1.14{\cdot}10^{-1}$	$C\text{-}mol_s{\cdot}m^{-3}$	This study
K_O	$1.13{\cdot}10^{-3}$	$mol_{O2}{\cdot}m^{-3}$	This study
$k_{OL}a$	$2.42{\cdot}10^{-3}$	s^{-1}	This study
m_O	44.41	–	This study
K_C	$1.00{\cdot}10^{-2}$	$C\text{-}mol{\cdot}m^{-3}$	This study
F_G^{in}	$3.33{\cdot}10^{-4}$	$m^3{\cdot}s^{-1}$	This study
V_G	0.24	m^3	This study
$k_{CL}a$	$2.21{\cdot}10^{-3}$	s^{-1}	This study
m_C	1.84	–	This study
τ	11.92	min	This study
ε_G	0.28	–	This study
$q_{O,hetmax}$	$4.08{\cdot}10^{-6}$	$mol_{O2}{\cdot}C\text{-}mol_x^{-1}{\cdot}s^{-1}$	This study

2.5. Stoichiometric model

Autotrophic CO_2 consumption associated to the aforementioned O_2 production was determined via the stoichiometric equation of autotrophic growth on ammonia. Because the elemental composition of *G. sulphuraria* has not been accurately described yet, we used as a reference the algal biomass elemental composition previously determined by Kliphuis et al. [18], normalized per C-mol: $CH_{1.62}O_{0.41}N_{0.14}P_{0.01}$. Consequently, for the production of 1 C-mol of biomass the autotrophic stoichiometry results in the following:

$$0.14\ NH_4^+ + 0.01\ H_2PO_4^- + 0.58\ H_2O + 1\ CO_2 \rightarrow CH_{1.62}O_{0.41}N_{0.14}P_{0.01} + 1.11\ O_2 + 0.13\ H^+. \quad (2)$$

Using this equation, the autotrophic yield of fixed CO_2 on O_2 ($Y_{C/O}$, $mol_{CO2}{\cdot}mol_{O2}^{-1}$) was calculated: 0.90 $mol_{CO2}{\cdot}mol_{O2}^{-1}$. Moreover, heterotrophic O_2 consumption and CO_2 production yields can also be determined via the stoichiometry of heterotrophic growth on ammonia. For this, the heterotrophic biomass yield on substrate ($Y_{x/s}^{het}$, $C\text{-}mol_x{\cdot}C\text{-}mol_s^{-1}$) must be known (Table 1). This parameter has been previously determined experimentally for the strain *G. sulphuraria* ACUF 064 growing on glucose [12]. Then, the equation becomes as depicted below, normalized for the production of 1 C-mol of biomass:

$$0.14\ NH_4^+ + 0.01\ H_2PO_4^- + 1.69\ CH_2O + 0.59\ O_2 \rightarrow CH_{1.62}O_{0.41}N_{0.14}P_{0.01} + 0.69\ CO_2 + 1.11\ H_2O + 0.13\ H^+. \quad (3)$$

As a result, the heterotrophic CO_2 yield on sugar ($Y_{C/s}$, $mol_{CO2}{\cdot}C\text{-}mol_s^{-1}$) and the heterotrophic O_2 yield on sugar ($Y_{O/s}$, $mol_{O2}{\cdot}C\text{-}mol_s^{-1}$) result in 0.41 $mol_{CO2}{\cdot}C\text{-}mol_s^{-1}$ and 0.35 $mol_{O2}{\cdot}C\text{-}mol_s$, in the order stated. If the heterotrophic O_2 consumption is made equal to the autotrophic production, the stoichiometric equation for *OBM* can be obtained by adding Equations (2) and (3). It should be emphasized that this approach assumes that mixotrophic productivity results from the simple addition of the autotrophic and the heterotrophic metabolisms. The sum results in the following expression, normalized for the production of 1 C-mol of biomass:

$$0.14\ NH_4^+ + 0.01\ H_2PO_4^- + 1.11\ CH_2O \rightarrow CH_{1.62}O_{0.41}N_{0.14}P_{0.01} + 0.11\ CO_2 + 0.53\ H_2O + 0.13\ H^+. \quad (4)$$

Because an excess of CO_2 is produced in the process, the system requires to bleed off-gas in order to avoid pressure buildup. The extent of this bleed flowrate is discussed in the next section, 2.6. Kinetic model. Besides CO_2 accumulation, there is also net proton production, which would result in the acidification of the medium. The model did not account for base addition because it was assumed that the pH fluctuations within a single daytime period were negligible. This is because in practice the system is buffered by the hydrogen sulfate-sulfate equilibrium.

2.6. Kinetic model

We established mass balances for sugar, O_2, CO_2 and inert gases over the gas and liquid phases of every *STR* to describe the evolution of the process in the *TPBR*. The equations include terms that account for component mass flows entering and leaving the *STR*, for gas–liquid mass transfer and for accumulation of the component within the *STR* volume. Together with these, autotrophic and heterotrophic production/

consumption terms were also included based on Monod kinetics. Autotrophic activity is made dependent on CO_2 concentration and heterotrophic activity is made dependent on the availability of O_2 and sugar. Cell maintenance was not considered in the model. The equations corresponding to the first and the *k*-th *STR* are included in this section. The value of the operational, physical and biological parameters used in these equations is stated in Table 1. Starting with sugar, the balances over the liquid phase go as follows:

$$\frac{dC_s^1}{dt} = \frac{F_L^{in}}{V_L/N}C_s^N + \frac{F_{FEED}}{V_L/N}C_{sFEED} - \frac{F_L^1}{V_L/N}C_s^1 - q_{smax}\frac{C_s^1}{C_s^1+K_s}\frac{C_{OL}^1}{C_{OL}^1+K_O}C_x, \quad (5)$$

$$\frac{dC_s^k}{dt} = \frac{F_L^{k-1}}{V_L/N}C_s^{k-1} - \frac{F_L^k}{\frac{V_L}{N}}C_s^k - q_{smax}\frac{C_s^k}{C_s^k+K_s}\frac{C_{OL}^k}{C_{OL}^k+K_O}C_x. \quad (6)$$

In these expressions, F_L^{in} stands for the initial liquid flowrate and F_L^{k-1} for the liquid flowrate in the (*k-1*)-th *STR* ($m^3 \cdot s^{-1}$). V_L stands for the total liquid volume in the *TPBR* (m^3) and C_s^N and C_s^{k-1} for the sugar concentration in the *N*-th and the (*k-1*)-th *STRs* ($C\text{-}mol_s \cdot m^{-3}$). The second term of Equation (5) defines the external sugar supply, where F_{FEED} is the glucose solution feed flowrate ($m^3 \cdot s^{-1}$) and C_{sFEED} is the concentration of glucose in the feed ($C\text{-}mol_s \cdot m^{-3}$). The latter was chosen at concentration of 200 g L^{-1}. In the third term, F_L^1 and C_s^1 are the liquid flowrate ($m^3 \cdot s^{-1}$) and the concentration of sugar ($C\text{-}mol_s \cdot m^{-3}$) in the first *STR*, respectively. F_L^k and C_s^k represent equivalent magnitudes in the *k*-th *STR*. Finally, the fourth term represents heterotrophic sugar consumption, where q_{smax} stands for the maximum specific sugar uptake rate ($C\text{-}mol_s \cdot C\text{-}mol_x^{-1} \cdot s^{-1}$). K_s is the half saturation constant for sugar ($C\text{-}mol_s \cdot m^{-3}$) and K_O denotes the half saturation constant for O_2 ($mol_{O2} \cdot m^{-3}$). C_{OL}^1 and C_{OL}^k are the concentration of O_2 in the liquid in the first and in the *k*-th *STRs*. In regard to O_2, mass balances must be established for both the liquid and gas phases. The first can be constructed in the following manner:

$$\frac{dC_{OL}^1}{dt} = \frac{F_L^{in}}{V_L/N}C_{OL}^N - \frac{F_L^1}{V_L/N}C_{OL}^1 + k_{OL}a\left(\frac{C_{OG}^1}{m_O} - C_{OL}^1\right) + q_{O,auto}\frac{C_{CL}^1}{C_{CL}^1+K_C}C_x - q_{smax}\,Y_{O/s}\,\frac{C_s^1}{C_s^1+K_s}\,\frac{C_{OL}^1}{C_{OL}^1+K_O}C_x \quad (7)$$

and

$$\frac{dC_{OL}^k}{dt} = \frac{F_L^{k-1}}{V_L/N}C_{OL}^{k-1} - \frac{F_L^k}{V_L/N}C_{OL}^k + k_{OL}a\left(\frac{C_{OG}^k}{m_O} - C_{OL}^k\right) + q_{O,auto}\frac{C_{CL}^k}{C_{CL}^k+K_C}C_x - q_{smax}\,Y_{O/s}\,\frac{C_s^k}{C_s^k+K_s}\,\frac{C_{OL}^k}{C_{OL}^k+K_O}C_x, \quad (8)$$

where C_{OL}^N and C_{OL}^{k-1} symbolize the O_2 concentration in the liquid at the *N*-th and the (*k-1*)-th *STRs*. The third term of the equations represents mass transfer between the gas and the liquid phases, where $k_{OL}a$ stands for the mass transfer coefficient of O_2 (s^{-1}). Also in this term, C_{OG}^1 and C_{OG}^k stand for the O_2 concentration in the gas phase in the first and the *k*-th *STR* ($mol \cdot m^{-3}$) and m_O is the partition coefficient of O_2. Proceeding to the O_2 production term, $q_{O,auto}$ represents the maximum specific autotrophic oxygen production rate ($mol_{O2} \cdot C\text{-}mol_x^{-1} \cdot s^{-1}$), as described previously in 2.4. Autotrophic oxygen production. C_{CL}^1 and C_{CL}^k depict CO_2 concentrations in the liquid of the first and the *k*-th *STR* ($mol_{CO2} \cdot m^{-3}$) and K_C is the half saturation constant for CO_2 ($mol_{CO2} \cdot m^{-3}$). The mass balances of O_2 over the gas phase resemble the liquid-phase equations without the parts related to biological activity:

$$\frac{dC_{OG}^1}{dt} = \frac{F_G^{in}}{V_G/N}C_{OG}^N - \frac{F_G^1}{V_G/N}C_{OG}^1 - k_{OL}a\left(\frac{C_{OG}^1}{m_O} - C_{OL}^1\right)\frac{V_L}{V_G}, \quad (9)$$

$$\frac{dC_{OG}^k}{dt} = \frac{F_G^{k-1}}{V_G/N}C_{OG}^{k-1} - \frac{F_G^k}{V_G/N}C_{OG}^k - k_{OL}a\left(\frac{C_{OG}^k}{m_O} - C_{OL}^k\right)\frac{V_L}{V_G}. \quad (10)$$

As per this equation, F_G^{in}, F_G^1, F_G^{k-1} and F_G^k stand for the initial gas flowrate and the gas flowrates in the first, (*k-1*)-th and *k*-th *STRs* ($m^3 \cdot s^{-1}$), in that order. V_G is the total gas volume in the *TPBR* (m^3) and C_{OG}^N and C_{OG}^{k-1} are the O_2 concentrations in the gas phase of the *N*-th and (*k-1*)-th *STRs* ($mol_{O2} \cdot m^{-3}$). The mass balances of CO_2 over the liquid and gas phases were constructed similarly:

$$\frac{dC_{CL}^1}{dt} = \frac{F_L^{in}}{V_L/N}C_{CL}^N - \frac{F_L^1}{V_L/N}C_{CL}^1 + k_{CL}a\left(\frac{C_{CG}^1}{m_C} - C_{CL}^1\right) - q_{O2auto}Y_{C/O}\frac{C_{CL}^1}{C_{CL}^1+K_C}C_x + q_{smax}\,Y_{C/S}\,\frac{C_S^1}{C_S^1+K_S}\,\frac{C_{OL}^1}{C_{OL}^1+K_O}C_x, \quad (11)$$

$$\frac{dC_{CL}^k}{dt} = \frac{F_L^{k-1}}{V_L/N}C_{CL}^{k-1} - \frac{F_L^k}{V_L/N}C_{CL}^k + k_{CL}a\left(\frac{C_{CG}^k}{m_C} - C_{CL}^k\right) - q_{O,auto}Y_{C/O}\frac{C_{CL}^k}{C_{CL}^k+K_C}C_x + q_{smax}\,Y_{C/S}\,\frac{C_S^k}{C_S^k+K_S}\,\frac{C_{OL}^k}{C_{OL}^k+K_O}C_x, \quad (12)$$

$$\frac{dC_{CG}^1}{dt} = \frac{F_G^{in}}{V_G/N}C_{CG}^N - \frac{F_G^1}{V_G/N}C_{CG}^1 - k_{CL}a\left(\frac{C_{CG}^1}{m_C} - C_{CL}^1\right)\frac{V_L}{V_G}, \quad (13)$$

$$\frac{dC_{CG}^k}{dt} = \frac{F_G^{k-1}}{V_G/N}C_{CG}^{k-1} - \frac{F_G^k}{V_G/N}C_{CG}^k - k_{CL}a\left(\frac{C_{CG}^k}{m_C} - C_{CL}^k\right)\frac{V_L}{V_G}. \quad (14)$$

In these expressions, $q_{O,auto}$ represents again the maximum specific autotrophic oxygen production rate, and C_{CL}^{k-1} and C_{CL}^N are the concentrations of CO_2 in the liquid ($mol \cdot m^{-3}$) of the (*k-1*)-th and *N*-th *STRs*. Conversely, C_{CG}^1, C_{CG}^k, C_{CG}^{k-1} and C_{CG}^N symbolize the gas concentrations for first, *k*-th, (*k-1*)-th and *N*-th *STRs* ($mol \cdot m^{-3}$). Concerning the mass transfer term, $k_{CL}a$ represents the mass transfer coefficient of CO_2 (s^{-1}) and m_C the partition coefficient of CO_2.

In order to solve all these balances, the initial conditions of the system must be set. Furthermore, F_L and F_G have to be determined for every *STR*. At the start, the *TPBR* was considered to be in equilibrium with air and F_{FEED} was 0. The initial flowrates, F_L^{in} and F_G^{in}, are operational parameters and were selected as $8.8 \cdot 10^{-4}$ and $3.3 \cdot 10^{-4}$ $m^3 s^{-1}$, respectively. These values are common operating conditions in our reference *TPBR* when operating the liquid and the gas pumps simultaneously (Fig. 1) and were also used for the *RTD* determination. These flow rates correspond to a linear velocity of nearly 0.4 $m \cdot s^{-1}$ for both the liquid and the gas phase. Thus, a general residence time can be defined (τ, s), which was measured in a preliminary study (Table 1).

In addition, the effect of hydrostatic pressure on the gas holdup (ε_G) was neglected and ε_G was considered equal and invariable for every *STR*. We also assumed that F_L remained constant throughout the *TPBR*. However, F_G cannot be considered constant because of the stoichiometry outlined in Equation (4) for *OBM*. If heterotrophic O_2 consumption equals autotrophic production, there will be a net CO_2 production and off-gas bleeding will become necessary to prevent pressure buildup in the system. F_G^1 and F_G^k can be obtained from a mass balance of all the gaseous components in the first and *k*-th *STRs*, provided that the total gas concentrations, C_{TG}^1 and C_{TG}^k are known ($mol \cdot m^{-3}$). To achieve this, balances over the inert fraction of the gas phase must be established beforehand:

$$\frac{dC_I^1}{dt} = \frac{F_G^{in}}{V_G/N}C_I^N - \frac{F_G^1}{V_G/N}C_I^1 \quad (15)$$

and

$$\frac{dC_I^k}{dt} = \frac{F_G^{k-1}}{V_G/N}C_I^{k-1} - \frac{F_G^k}{V_G/N}C_I^k, \quad (16)$$

where C_I^1, C_I^k, C_I^{k-1} and C_I^N are the inert gas concentrations in the first, *k*-th, (*k-1*)-th and *N*-th *STRs* ($mol \cdot m^{-3}$). With these, C_{TG}^1 and C_{TG}^k can be calculated:

$$C_{TG}^1 = C_{OG}^1 + C_{CG}^1 + C_I^1, \quad (17)$$

$$C_{TG}^{k} = C_{OG}^{k} + C_{CG}^{k} + C_{I}^{k}. \quad (18)$$

Then, by assuming steady state in the gas phase, we can describe a total mass balance over this phase and calculate F_G^1 and F_G^k:

$$F_G^1 = \frac{F_G^{in} C_{TG}^N - k_{OL}a\left(\frac{C_{OG}^1}{m_O} - C_{OL}^1\right)\frac{V_L}{N} - k_{CL}a\left(\frac{C_{CG}^1}{m_C} - C_{CL}^1\right)\frac{V_L}{N}}{C_{TG}^1}, \quad (19)$$

$$F_G^k = \frac{F_G^{k-1} C_{TG}^{k-1} - k_{OL}a\left(\frac{C_{OG}^k}{m_O} - C_{OL}^k\right)\frac{V_L}{N} - k_{CL}a\left(\frac{C_{CG}^k}{m_C} - C_{CL}^k\right)\frac{V_L}{N}}{C_{TG}^k}, \quad (20)$$

and the bleed flowrate (F_{BLEED}, $m^3 \cdot s^{-1}$). For this calculation, the gas flowrate in the N-th STR (F_G^N, $m^3 \cdot s^{-1}$) needs to be determined in advance following the procedure for F_G^k:

$$F_{BLEED} = F_G^N - F_G^{in}. \quad (21)$$

2.7. Simulation scenarios

In total, we simulated three different scenarios by adjusting O_2 production and glucose feeding: (1) simplified conditions with constant O_2 production, (2) clear sky and (3) cloudy weather. For (1) we used the aforementioned empirical $q_{O,auto}$ (see 2.4. Autotrophic oxygen production) and C_x at a constant rate during the simulation. In this scenario, F_{FEED} was also constant, corresponding to the amount of glucose feed required by the biomass to achieve OBM. This "stoichiometric" F_{FEED} was denominated F_{SFEED} ($m^3 \cdot s^{-1}$) and was calculated as follows:

$$F_{SFEED} = \frac{q_{O,auto} C_x V_L}{Y_{O/s} C_{sFEED}}. \quad (22)$$

In scenario (2), $q_{O,auto}$ was converted to a sinusoidal wave to mimic a clear sky day from sunrise to sunset (Fig. 2). The value of the daily averaged $q_{O,auto}$ was the same as for scenario (1). Lastly, for scenario (3) we used photosynthetically active radiation (PAR) data at ground level from a cloudy day at our reference $TPBR$ location (Bennekom, the Netherlands). The data was retrieved as global horizontal irradiance ($W \cdot m^2$) from the National Solar Radiation Database (https://nsrdb.nrel.gov/) and converted into PAR by using a conversion factor of 0.45. The retrieved data corresponded to the 15th of August of 2019. This day was selected due to the irregular light pattern exhibited in the PAR data. $q_{O,auto}$ was derived from these data by normalizing the radiation curve to the sinusoidal function from scenario (2), assuming a linear relationship between PAR irradiance and O_2 production (Fig. 2). In scenarios (2) and (3), F_{FEED} was set to 10 % of F_{SFEED} during the first residence time τ and henceforth adjusted automatically by the control system. In this way, there is sufficient CO_2 generated by heterotrophy to initiate photosynthesis and activate the control strategy. The simulations under simplified conditions focused on a time frame of 16 h, the maximum daytime length in the Netherlands. On the other hand, the clear sky and cloudy weather simulations lasted 14.5 h, which corresponds with the length of the selected day for scenario (3).

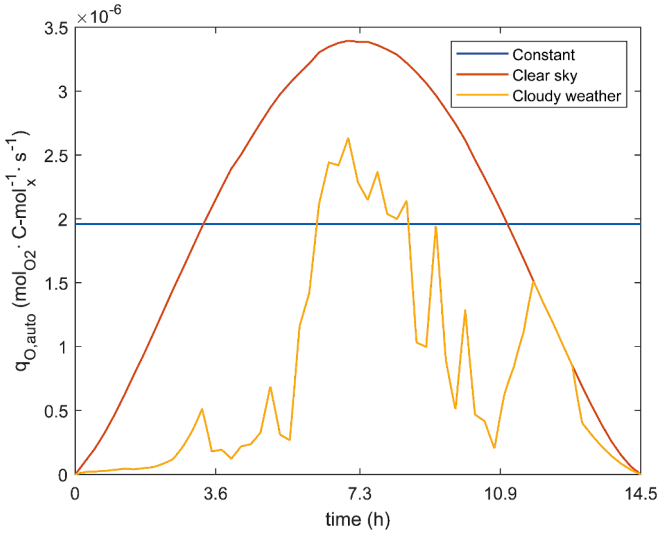

Fig. 2. Autotrophic oxygen production patterns during 14.5 h daytime in the simulated scenarios: constant (blue), clear sky (orange) and cloudy weather (yellow). (For interpretation of the references to colour in this figure legend, the reader is referred to the web version of this article.)

2.8. Controller design

Two types of control strategies based on a proportional-integral-derivative (PID) controller were implemented in the model: a low-frequency constant setpoint and a high-frequency variable setpoint control strategies. Both strategies aimed at maintaining the concentration of O_2 in the gas phase (C_{OG}, $mol \cdot m^{-3}$) at a stable level, but differed in the error definition. The manipulated variable (MV) was F_{FEED} in both cases. In the first type of strategy, control action over the MV was executed every τ (i.e. low-frequency) and the control output was kept constant for the following τ. In this way, the control action is based on a single fluid element and is implemented every time this element passes through the outlet of the tube. The value of C_{OG} at the N-th STR is compared to the setpoint concentration value, expressed as a volume fraction ($C_{OG,sp}$, −), and the error signal (e, −) is calculated as a feedback deviation:

$$e(t) = C_{OG}^N(t) - C_{OG,sp}^N, \text{ where } t = k\tau \text{ and } k \in \mathbb{N}. \quad (23)$$

On the other hand, the second type of control strategy consisted on exerting control action every second (i.e. high-frequency). In this strategy, the setpoint is not defined by the operator but it is rather dependent on C_{OG}. The value of C_{OG}, expressed as a concentration ($mol \cdot m^{-3}$), was continuously compared with its value at the previous τ and the e ($mol \cdot m^{-3}$) was computed accordingly:

$$e(t) = C_{OG}^N(t) - C_{OG}^N(t-\tau), \text{ where } t > \tau,\ t = k \cdot 1\,s \text{ and } k \in \mathbb{N}. \quad (24)$$

In the following sections, e was recalculated as volume percentage (% vol) to more easily compare the results of the two control strategies. The initial PID parameters were determined by the Ziegler-Nichols' ultimate gain method [19]. The value of the proportional gain coefficient (K_P) was manually increased in a step-wise manner until a stable and consistent oscillatory C_{OG} response was found under constant light conditions. The K_P causing that response corresponds to the ultimate gain coefficient ($K_{P,u}$), and its period corresponds to the ultimate period (P_u). The K_P, integral term (τ_I), and derivative term (τ_D) for the PI and PID controllers were determined based on $K_{P,u}$ and P_u using the relationships outlined by Ogunnaike and Ray [20]. The P controller was not considered because of the offset generated in a closed loop system. The controllers were implemented with a low-frequency error definition and compared under constant light. The controller demonstrating superior performance was subsequently used for the outdoor weather simulations using both error definitions: low-frequency and high-frequency. The PID parameters used in the high-frequency strategy underwent additional refinement through manual adjustments. This iterative process aimed to achieve a response that maintained DO levels above 10 % in simulations with constant light.

2.9. Numerical methods

In this study, the model equations and the associated control strategies were implemented and solved using MATLAB R2020a

(Mathworks, USA). The system involved solving a matrix comprising 6 *N* balances simultaneously, out of which 5 *N* were nonlinear. The numerical solution was obtained using MATLAB's built-in function, ode45. Depending on the control strategy employed, time step for each integration of the solver was adjusted accordingly. For simulations conducted under simplified conditions, a time step of 10 s was utilized. For simulations employing the low-frequency control strategy, the time step was τ. Lastly, simulations with the high-frequency control strategy used a time step of 1 s.

2.10. Physical and biological parameters estimation

The determination of V_L, ε_G and V_G started by measuring the water required to fill the reference *TPBR* with a flowmeter. The filling was performed under the same flow configuration used in the other parts of the study. The resulting total liquid volume (V_{LT}, m^3) from the measurement was adjusted by deducting the liquid volume in the collection vessel (V_v, m^3). In this way, V_L can be obtained:

$$V_L = V_{LT} - V_v. \tag{25}$$

Subsequently, the liquid holdup (ε_L) and the ε_G in the tubular section were calculated:

$$\varepsilon_L = \frac{V_L}{V_T}, \tag{26}$$

$$\varepsilon_G = 1 - \varepsilon_L. \tag{27}$$

Here, V_T represents the total volume of the tube (m^3). V_G can be then derived utilizing ε_G:

$$V_G = V_T\,\varepsilon_G. \tag{28}$$

The transport properties of the system were included in the model via $k_{OL}a$, $k_{CL}a$ and the partition coefficients, m_O and m_C. The mass transfer coefficients were measured in the reference *TPBR* at 20 °C following the steady state method described in detail in Appendix 1. In a nutshell, pure N_2 gas was sparged into the collection vessel of the *TPBR*, dropping the *DO* below air saturation, and the liquid was recirculated. O_2 mass transfer then occurred along the tube, from the freshly supplied air to the liquid. The *DO* difference was measured by two *DO* probes, located at different parts of the tube (Fig. 1).

Before implementation in the model, $k_{OL}a$, $k_{CL}a$ were adjusted to the process running temperature, 37 °C. We considered that the main factor affecting mass transfer was the increase in gas–liquid diffusivity (D_{GL}, $m^2{\cdot}s^{-1}$) due to the rising temperature and decreasing liquid dynamic viscosity (μ_L, Pa·s) [21]. The proportional increase in D_{GL} due to increasing temperature (T, K) and decreasing μ_L was calculated following Wilke and Chang's relationship:

$$D_{GL} \propto \frac{T}{\mu_L}, \tag{29}$$

resulting in a factor of 1.7. In addition, considering Higbie's penetration theory, the mass transfer coefficient (k_L, s^{-1}) is proportional to the square root of D_{GL} divided by the contact time between phases (τ_C, s):

$$k_L \propto \sqrt{\frac{D_{GL}}{\tau_C}}, \tag{30}$$

and thus k_L increases by a factor 1.3 when increasing T from 20 to 37 °C. The value of m_O and m_C used in the model was obtained and adapted to 37 °C based on the procedure explained by Sander [22].

Besides assessing the volume and transport properties, the Monod kinetics parameters of *G. sulphuraria* ACUF 064 were determined experimentally. Specifically, we measured q_{smax}, K_s and K_O. The determination was carried out via respirometric measurements in a Hansatech Oxygraph + biological oxygen monitor (*BOM*) (Hansatech, UK). The comprehensive procedures for obtaining each parameter are outlined in Appendix 2.

2.11. Scale-down reactor configuration

Model simulations of a *TPBR* operated under *OBM* were validated in a lab-scale setup using a scale-down approach. A schematic representation of the setup is depicted in Appendix 3. The reactor used in the study was an *STR* with a total volume of 3 L and a working volume of 2 L. The cylindrical vessel was surrounded by an octagon of vertical light panels that ensured homogeneous illumination, as explained meticulously in a previous study [14]. Throughout the experiments, the culture was continuously stirred at 500 rpm. pH was maintained at 1.8 by manual addition of 2 M NaOH. Temperature was maintained at 37 °C via a heat exchanger, and evaporation was prevented with a condenser fed with water at 2 °C. A gas recycle line was installed after the condenser to mimic gas recirculation in the *TPBR*. The recycling gas flowrate was 0.102 L min^{-1} so as to reproduce the measured $k_{OL}a$ in the *TPBR*. This value was estimated from a previous $k_{OL}a$ measurement in the reactor [23], assuming a linear correlation between gas flowrate and $k_{OL}a$ if the stirring rate remains the same.

Additionally, the pressure of the system was set to 10 mbar to prevent mixing of the off-gas with external air. This was achieved by employing a water lock placed after the condenser. We monitored any deviations from this pressure by a manometer. The outlet gas in the recycle line was compressed back into the *STR* by means of a diaphragm gas pump. Gas flowrate was adjusted with a mass flow controller TMF 5800S (Brooks Instruments, the Netherlands) before entering the reactor via the sparger. Fresh air and air enriched with CO_2 were provided when required by disconnecting the recycle line. Two Visiferm DO ECS 225 sensors (Hamilton, USA) were installed in the liquid phase and in the recycle line to monitor *DO* and C_{OG}, respectively. Both sensors were calibrated by sparging with N_2 and air to obtain 0 % and 100 % air saturation readings, respectively.

2.12. Strain, medium and inoculum growth conditions

The validation experiments were carried out with *Galdieria sulphuraria* ACUF 064 (http://www.acuf.net), donated by Prof. A. Pollio (University of Naples, Italy). The medium used for the cultivation of this strain had the following composition (mol·L^{-1}): $8.0{\cdot}10^{-2}$ $(NH_4)_2SO_4$, $6.5{\cdot}10^{-3}$ $MgSO_4{\cdot}7H_2O$, $4.7{\cdot}10^{-4}$ $CaCl_2{\cdot}2H_2O$, $6.3{\cdot}10^{-4}$ $FeCl_3{\cdot}6\ H_2O$, $1.2{\cdot}10^{-2}$ H_3PO_4, $1.7{\cdot}10^{-3}$ NaCl, $8.1{\cdot}10^{-3}$ KCl, $8.0{\cdot}10^{-4}$ H_3BO_3, $8.1{\cdot}10^{-5}$ $MnCl_2{\cdot}4H_2O$, $8.2{\cdot}10^{-5}$ $ZnCl_2$, $3.2{\cdot}10^{-5}$ $CuSO_4{\cdot}5H_2O$, $1.7{\cdot}10^{-5}$ $Na_2MoO_4{\cdot}2H_2O$ and $1.7{\cdot}10^{-5}$ $CoCl_2{\cdot}6H_2O$. pH was adjusted to 1.8 with H_2SO_4. The inoculum for the experiments was obtained by cultivating previously cryopreserved cells in a 250-mL flask containing 100 mL of medium at 37 °C, 2 % v/v CO_2, 120 rpm and a light intensity of 100 $\mu mol{\cdot}m^{-2}{\cdot}s^{-1}$.

2.13. Validation experiments

After inoculating the reactor, the culture was grown autotrophically in batch mode until C_x reached 3 g·L^{-1}. Throughout this phase, the *PFD* was gradually increased from 150 µmol $m^{-2}{\cdot}s^{-1}$ to a final value of 500 µmol $m^{-2}{\cdot}s^{-1}$ to prevent photoinhibition. This final *PFD* was maintained until the end of the experiments. Subsequently, a 100 g·L^{-1} glucose solution was fed to the reactor at a rate of 1.1 g·h^{-1} for 1 day to acclimate the cells to mixotrophy. Following this adaptation period, aeration was halted and *DO* levels were maintained at 105 % air saturation via automatic glucose feeding. This condition was sustained until C_x reached 8 g·L^{-1}, at which point dilution was initiated at a rate of 0.2 day^{-1}. After 3 days of chemostat, the first validation experiment commenced.

Initially, the system was aerated for 2 h at a flowrate of 1 Lmin^{-1} to attain equilibrium with air. Then, gas recycling was activated and the

reactor was operated in batch mode while a glucose solution of 150 $g{\cdot}L^{-1}$ was supplied discontinuously (i.e. in pulses) over 16 h. Pulse feeding was regulated by means of a *PID* controller that manipulated the glucose pump flow rate to maintain a fixed setpoint for C_{OG}. The controller was active for 7 s every 700 s, corresponding to the τ in the first hypothetical *STR* and in the entire *TPBR*, respectively. After the 16-hour simulated daytime, dilution was resumed at 0.2 day^{-1} and continued for at least 3 days. Two additional validation replicates were conducted in a similar manner.

3. Results and discussion

3.1. Number of stages determination

The optimal number of tanks (*N*) value corresponding to our reference tubular photobioreactor (*TPBR*) with two-phase wavy flow needed to be estimated to be able to construct a model following the tank in series (*TIS*) approach. One way to accomplish this is by looking at the residence time distribution (*RTD*) of such *TPBR*. Our study delved into the *RTD* of our system by means of a pulse input experiment using HCl as tracer. The experimental *RTD* function *E(t)* from each replicate was plotted against the corresponding function of the *TIS* model for different values of *N* (Fig. 3).

The sharp shape of the experimental curves implies that the pH data acquisition did not have sufficient resolution to represent the pulse input accurately and the top of the peak might have occurred between the registered points. Despite this limitation in resolution, the experimental *RTD* curves suggest that axial dispersion is overall low in the reference *TPBR* as shown by the size of the distribution tails. Furthermore, the curves also indicate that the system can be approached with different extents of accuracy with *TIS* model by using an *N* on the order of tens to hundreds. We checked this conclusion by means of a model sensitivity analysis that compares the results for sugar, oxygen (O_2), carbon dioxide (CO_2) and inert gas concentrations with 100, 500 and 1000 *STRs* (Appendix 4). The concentration profiles are very similar and the error incurred by using 100 instead of 500 or 1000 is very low. Accordingly, we finally selected an *N* of 100 for the rest of the simulations in this study as this number offers a good balance of accuracy and simulation time.

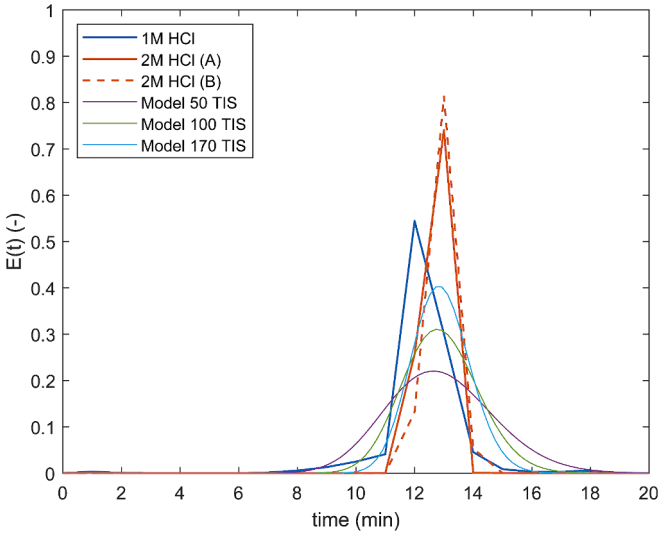

Fig. 3. Experimental *RTD* functions from the experiments with 1 M HCl (blue, solid), 2 M HCl (A) (orange, solid) and 2 M HCl (B) (orange, dashed) compared with the *RTD* of the *TIS* model with 50 (purple), 100 (green) and 170 (light blue) ideal *STRs*. (For interpretation of the references to colour in this figure legend, the reader is referred to the web version of this article.)

3.2. Model simulation under simplified conditions

Understanding the behaviour of the model under simplified conditions is crucial for the interpretation of the following simulations with complex light inputs and active control strategies. Accordingly, we first ran a simulation assuming constant light for 16 h, and thus constant autotrophic O_2 production, and constant glucose solution feed flowrate (F_{FEED}). This fixed F_{FEED} was defined as the amount of glucose required to achieve oxygen-balanced mixotrophy (*OBM*) for the selected biomass concentration (C_x), denominated F_{SFEED} (Eq. (22)). The calculation yielded a value of F_{SFEED} at 0.37 L h^{-1}, equivalent to a volumetric glucose supply rate of 1.92 $kg{\cdot}m^{-3}{\cdot}day^{-1}$. The results of the simulation for the most relevant process variables are plotted as a function of tube length and simulation time in Fig. 4.

The concentration of glucose (C_s) showed a stable profile over time after an initial short period of increase along the tube (Fig. 4A). The maximum C_s was reached at the beginning of the tube, where sugar is fed, and then decreased progressively until being completely depleted by the end of the tube. Glucose depletion implies that cell metabolism was not constantly mixotrophic. Having a glucose gradient matches the expected plug flow fluid behaviour of the *TPBR*, as there is only one substrate feeding point at the starting point of the tube. On the other hand, the concentration of CO_2 in the gas (C_{CG}) rose linearly to 17.9 % v/v as time proceeded (Fig. 4B). Accumulation of CO_2 is expected based on the stoichiometry of *OBM*, as O_2 and CO_2 cannot be balanced simultaneously due to slightly different stoichiometric coefficients.

Dissolved oxygen (*DO*) concentration peaked at 120.1 % air saturation at both the beginning and end of the tube during the initial phase of the simulation (Fig. 4C). In the middle section of the tube, glucose consumption led to a drop in *DO* below saturation levels. This parabolic pattern follows the results obtained for C_s. As glucose is utilized, *DO* decreases until C_s is entirely depleted, after which *DO* levels rise again. Interestingly, *DO* levels at every point of the tube declined over time, never reaching a stable level. The concentration of O_2 in the gas (C_{OG}) displayed a uniform decreasing trend along the entire length of the tube (Fig. 4D). By the end of the simulated day, *DO* and C_{OG} had reached minima of 60.7 % air saturation and 16.1 % v/v, respectively. This pattern can be attributed to the accumulation of CO_2 in the gas phase, but it might also suggest that there was net O_2 consumption in the reactor. In such case, the heterotrophic metabolism would have dominated over its autotrophic counterpart. In principle, by providing F_{SFEED} we could expect to balance O_2 production and consumption.

In conditions devoid of constraints, the maximum autotrophic specific O_2 production rate is $q_{O,auto}$, at $1.96{\cdot}10^{-6}$ $mol_{O2}{\cdot}C\text{-}mol_x^{-1}{\cdot}s^{-1}$ (Table 1). Conversely, the maximum heterotrophic specific O_2 consumption, $q_{O,hetmax}$ ($mol_{O2}{\cdot}C\text{-}mol_x^{-1}{\cdot}s^{-1}$), can be derived from the maximum specific sugar uptake rate (q_{smax}) and $Y_{O/s}$ (Table 1), resulting in a value of $3.33{\cdot}10^{-6}$ $mol_{O2}{\cdot}C\text{-}mol_x^{-1}{\cdot}s^{-1}$. This is almost 2 times higher than $q_{O,auto}$, a discrepancy that implies that heterotrophic metabolism dominates when not significantly limited. The extent of the limitations in this simulation becomes apparent when examining the spatially averaged Monod terms, illustrated in Appendix 5. Despite heterotrophic O_2 consumption being restricted to approximately 52 % of its capacity due to substrate limitation, it still surpassed autotrophic O_2 production. This difference diminished over time as the marginal CO_2 limitation on the photosynthetic metabolism disappeared due to glucose oxidation.

The resulting decrease in *DO* drove O_2 transfer from the gas to the liquid phase, contributing to the observed reduction of C_{OG}. However, the transfer rate was not sufficient to balance O_2 consumption in the liquid phase during the simulated 16-hour daytime. Besides transfer to the liquid phase, the decrease in C_{OG} was also influenced by the progressive accumulation of CO_2 in the gas phase, steered by the aforementioned metabolic imbalance. The bleed gas flowrate is adjusted so that the recirculated gas inlet flowrate does not increase due the net production of CO_2 caused by the aforementioned metabolic imbalance. The bleed gas composition and flowrate throughout the simulation are

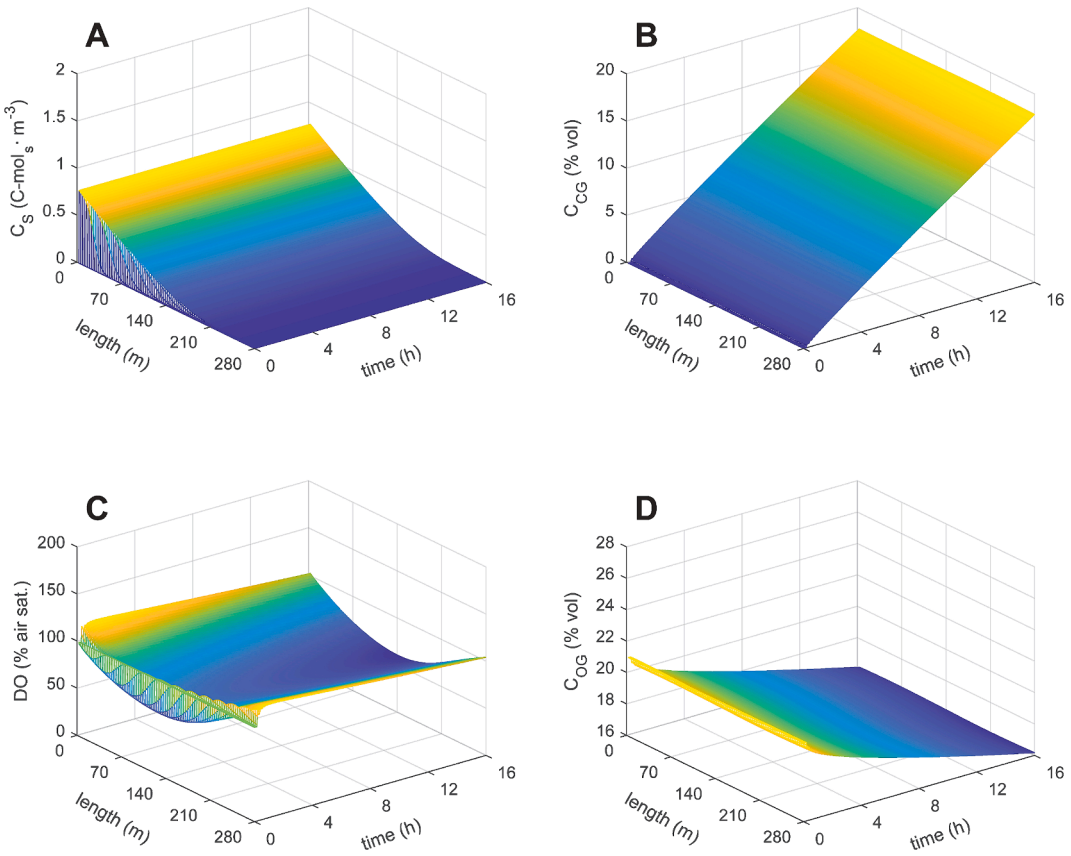

Fig. 4. Model predictions for C_s (A), C_{CG} (B), *DO* (C) and C_{OG} (D) under simplified conditions.

depicted in Appendix 6. The existence of the bleed gas implies that O_2 balance can never be reached with a F_{FEED} solely based on stoichiometry, as part of the O_2 is lost in a non-biological process.

3.3. Controller design for clear sky and cloudy weather conditions

When dealing with real outdoor conditions, F_{FEED} must be carefully adjusted over time to match the dynamic autotrophic O_2 production so as to achieve *OBM*. If there is too much glucose input, *DO* might drop below 10 % air saturation and cause harmful effects to the biomass [16]. Conversely, providing insufficient glucose might cause CO_2 limitation for photosynthesis and lead to low biomass productivities. In order to get an adequate response, we designed and compared various control strategies that were based on a *PID* controller. This type of controller, known for its simplicity and versality, is one of the most used in industry, including in the control of chemical and biological processes [24]. We chose C_{OG}, instead of *DO*, as the variable to be controlled. Although the latter might offer a more immediate response, the signal might be noisier due to sudden changes in the liquid, where the biological activity occurs. In turn, C_{OG} offers a more stable signal in exchange for some sluggishness due to the delay caused by mass transfer and mixing.

The first step in controller design is determining the *PID* parameters so that the response of the controller is adequate for the behaviour of *OBM*. For this purpose, we followed the classic controller tuning method proposed by Ziegler and Nichols, commonly called the ultimate gain method. This method was implemented for the low-frequency control strategy, explained comprehensively in 2.8. Controller design, with a setpoint of 18 % v/v of O_2. The parameters derived from this strategy were extrapolated to the high-frequency controller, given that simulations with the latter proved to be significantly more computationally intensive. It is important to note that this work did not focus on *PID* tuning. Thus, while this method may provide a convenient initial approach, future research could explore more effective tuning methods, such as the one-third rule or the simplified internal model control (*SIMC*). The resulting ultimate proportional gain coefficient ($K_{P,u}$) and ultimate period (P_u) for the C_{OG}-based controller were $1.16{\cdot}10^{-5}$ (−) and 3600 s, respectively. A graphical representation of the oscillatory response obtained with these parameters is reported in Appendix 7. After finding $K_{P,u}$ and P_u, the proportional gain coefficient (K_P), the integral term (τ_I) and the derivate term (τ_D) were subsequently derived for the low-frequency *PI* (K_P and τ_I equal to $5.22{\cdot}10^{-6}$ (−) and 3000 s^{-1}, respectively) and the *PID* controllers (K_P, τ_I and τ_D equal to $6.96{\cdot}10^{-6}$ (−), 1800 s^{-1} and 450 s, respectively). Then, these controllers were implemented in the model with the calculated parameters and their performances were compared under constant light (Fig. 5). For the sake of visualization, only the C_{OG} at the end of the tube is represented over time. The performance was evaluated based on the following criteria: (1) stability should be reached rapidly with minimal oscillations, (2) *DO* should remain above 10 % air saturation and (3) setpoint offset should be as low as possible. Further to this, we defined stability as oscillations that are no more than ± 2 % of the setpoint.

In the simulation with the *PI* controller, C_{OG} reached the setpoint within the accepted range of stability after 4.5 h. In comparison, with the *PID* controller C_{OG} was stable after 3 h at the expense of a deeper initial oscillation. Based on these results, the *PID* controller was chosen as the best strategy for being the fastest achieving stability while keeping a reasonable oscillation profile.

The performance of the *PID* controller with low-frequency and high-frequency error definitions was assessed under outdoor light conditions to determine its suitability for implementation at pilot scale. We tested two scenarios: a day with perfect clear sky and a cloudy summer day measured in the surroundings of our reference *TPBR*. In these simulations, differently to the previous sections, the length of the day was adjusted 14.5 h. This daytime length corresponds to the August summer

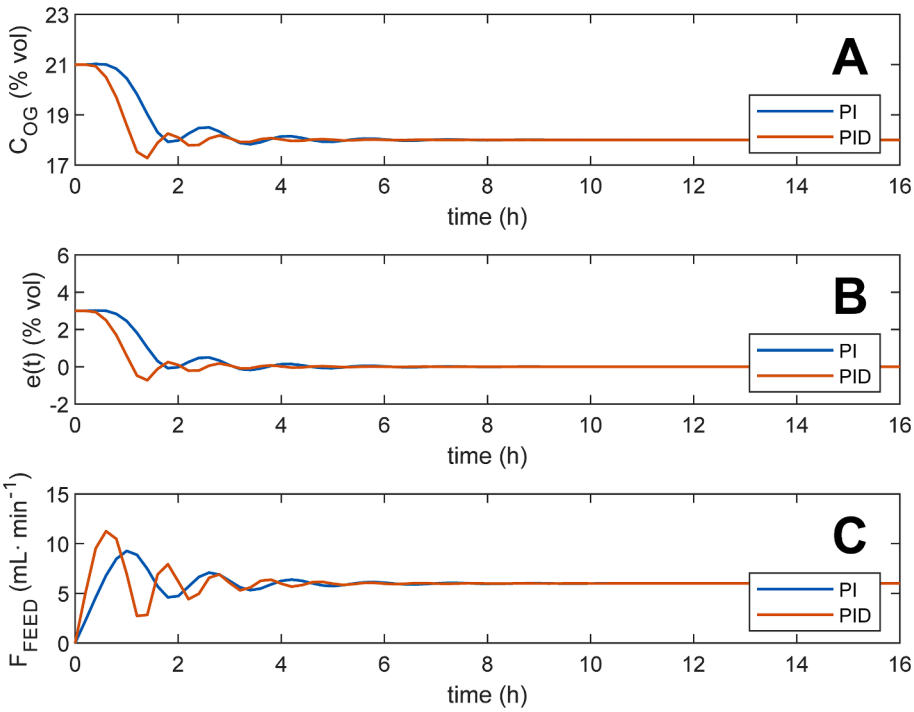

Fig. 5. Controller comparison results for C_{OG} (A), *e(t)* (B) and F_{FEED} (C) at the end of the tube under constant light conditions with the low-frequency error definition. *PI* is depicted in blue and *PID* in red. (For interpretation of the references to colour in this figure legend, the reader is referred to the web version of this article.)

day that was used as an example of a day with irregular cloud cover. The setpoint for C_{OG} was selected as 18 % v/v, where applicable. Furthermore, during the first tube circulation time τ, F_{FEED} was set to 10 % of the stoichiometric flowrate to avoid CO_2 limitation at the beginning of the simulation. In this way, the startup of the control system is not limited by the low initial CO_2 concentration, which is dictated by equilibrium with

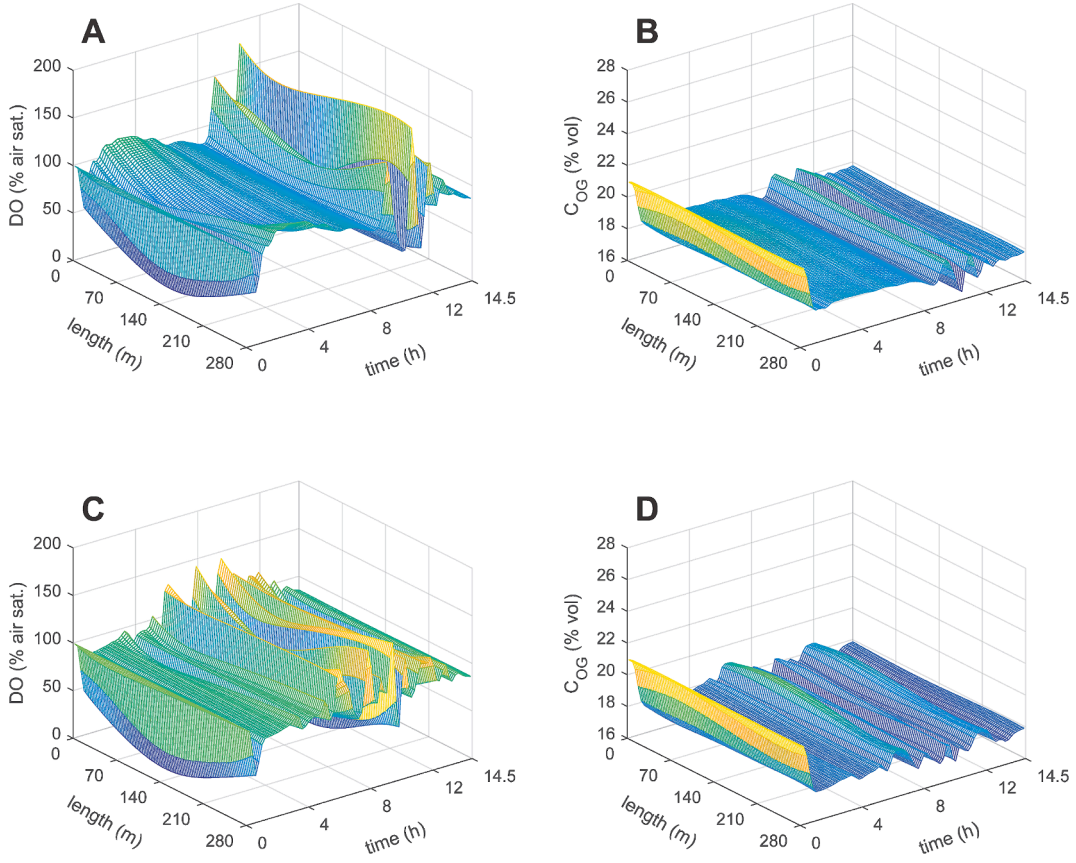

Fig. 6. Model predictions for *DO* and C_{OG} under clear sky conditions (A, B) and cloudy weather (C, D) with the low-frequency control strategy.

air reached during the hypothetical preceding night period.

Prior to conducting the definitive simulations with the high-frequency strategy and dynamic $q_{O,auto}$, further refinement of the *PID* parameters was performed. Initial simulations with a constant $q_{O,auto}$, employing the parameters derived directly from the ultimate gain method, revealed oscillations persisting below the 10 % *DO* threshold (data not shown). This result is in agreement with the fact that the ultimate gain method was applied to the low-frequency controller, which operates differently. To rectify this, an optimization process was conducted by trial and error under constant light conditions, focusing on reducing volatility in the oscillations. This was predominantly achieved by decreasing K_P and τ_D. The final optimized values for the high-frequency controller were determined as $3.5{\cdot}10^{-7}$ $m^6{\cdot}mol^{-1}{\cdot}s^{-1}$ for K_P, 2000 s^{-1} for τ_I and 47 s for τ_D. These values were then applied in the final simulations encompassing both the clear sky and cloudy weather scenarios.

3.4. Model simulations under clear sky and cloudy weather conditions

Starting with the results of the low-frequency strategy, *DO* showed an irregular oscillatory behaviour in both climatic scenarios (Fig. 6A and C). For most of the day, it remained above 10 % air saturation, reaching minima of 14.1 and 9.0 % during the morning of the clear sky and the cloudy weather conditions, in that order. On the other hand, the *DO* peaks reached levels of around 180 %. The response surface appeared more uneven under cloudy weather, which is attributed to the more irregular light pattern prevalent in this condition. Deeper oscillations coincided with the midday period, the moment of highest $q_{O,auto}$ input. C_{OG} appears more stable than *DO*, oscillating around the chosen setpoint of 18 % v/v (Fig. 6B and D). In both conditions there is first a decrease of C_{OG} before stabilizing after 1 h. Further oscillations appear in the periods when light intensity is changing more rapidly that undershoot the setpoint, resulting in values of 16.1 and 16.8 % v/v. This phenomenon occurs especially when C_{OG} decreases after reaching the maximum value in the clear sky condition or when there are fast changes in cloud cover. The error signal and the feed flowrate in this simulation are reported in Appendix 8.

The glucose concentration C_s exhibited a consistent pattern observed in both clear sky and cloudy day simulations (Appendix 8). At the beginning and end of the day, it was virtually 0, while during the middle part of the day there was a steep increase at the initial segment of the tube. This peak occurred simultaneously with the moment of highest light input and resulted from the controller response to the rapidly increasing O_2 production, emulating the behaviour of C_{OG}. Moreover, the C_s peak was almost twofold higher in the clear sky simulation than in the cloudy day, aligning with the lower average $q_{O,auto}$ from the latter. The volumetric glucose feeding rates during the clear sky and cloudy weather scenarios were 1.77 $kg{\cdot}m^{-3}{\cdot}day^{-1}$ and 0.75 $kg{\cdot}m^{-3}{\cdot}day^{-1}$, respectively. In the first scenario, this quantity is equivalent to the rate of glucose fed under simplified conditions for a similar time period of 14.5 h. Furthermore, 0.75 $kg{\cdot}m^{-3}{\cdot}day^{-1}$ correspond to a 60 % reduction, analogous to the reduction in $q_{O,auto}$ with cloudy weather.

These results suggest that the controller can supply the same amount of glucose for equivalent light inputs even if they are dynamic. However, this strategy resulted in a considerable C_s accumulation, maybe partially due to the choice of a C_{OG} setpoint of 18 % v/v. Large sugar gradients might be undesirable due to metabolic side effects in the biomass. As expected due to stoichiometry, C_{CG} increased progressively over time for both simulated conditions. The rate of accumulation was higher in the middle of day, when the majority of the glucose is supplied and oxidized (Appendix 8).

The outcomes of the high-frequency controller are represented in Fig. 7. In broad terms, the trends observed for all the compared process variables closely aligned with the results obtained with the low-

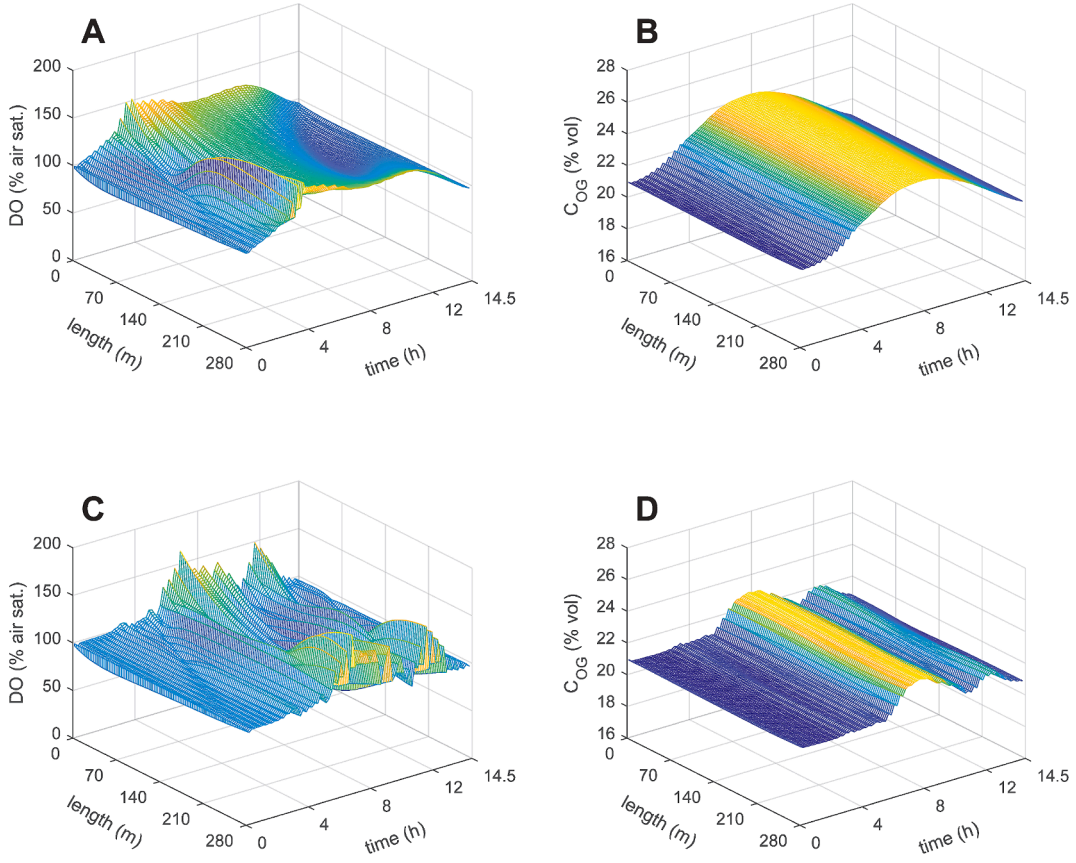

Fig. 7. Model predictions for *DO* and C_{OG} under clear sky conditions (A, B) and cloudy weather (C, D) with the high-frequency control strategy.

frequency control strategy in both climatic conditions. During the clear sky scenario, the glucose supply rate was 1.60 kg·m^{-3}·day^{-1} while in the cloudy weather condition this amount was 0.65 kg·m^{-3}·day^{-1}. This translates into slightly lower biomass productivity than the low-frequency strategy, accompanied by a lower degree of C_s accumulation (Appendix 9). Moreover, the high-frequency control showed a lower oscillation range of *DO*, fluctuating between 70.1 % and 162.1 % in the clear sky scenario and between 55.9 % and 167.0 % in the cloudy weather equivalent (Fig. 7A and C). Notably, with this strategy C_{OG} exhibited a slightly lower oscillation range, remaining between 20.9 and 24.3 % v/v in the clear sky scenario and between 20.8 and 23.1 % v/v in the cloudy weather condition (Fig. 7B and D). In general, the response from the high-frequency system deals more subtly with changes at a slight performance cost, as indicated by the obtained *DO* and C_{OG} ranges and the higher *DO* minimum. This response is advantageous in situations where dynamic conditions are the norm and not the exception. Moreover, from a control perspective, achieving the setpoint is not the primary focus but rather having stability while maintaining a good performance.

Despite the successful design and implementation of these controllers, the evolution of the aforementioned parameters in outdoor light simulations displayed a more irregular pattern than in the simplified conditions scenario. This showcases the importance of having an adequate initial F_{FEED} and a finely tuned controller response to prevent periods of either limiting or excessive sugar input into the system. While the control was not perfect and some oscillations persisted, it demonstrated the capability of the implemented controllers to handle real-life conditions. These controllers lay the foundation for the scale-up of *OBM* to pilot scale. The high-frequency strategy appears more promising for this task, although further refinement and tuning of the *PID* parameters are still recommended. It is also relevant to stress that the design of this control system was performed by trial and error. More efficient and robust designs could be implemented as well in the simulations. However, since we were satisfied with the initial results of this control strategy in terms of *DO* and C_{OG} ranges, we decided not to optimize this control system further.

3.5. Model validation

The predictions of the *PID* controller *in silico* were validated empirically in a lab-scale *STR* following a scale-down approach, a strategy that has already been explained elsewhere [16]. The passage of time in the *STR* represents the progression of a fluid element in the tubular section of the reference *TPBR*. In this way, the model can be validated without the need for time-consuming and expensive pilot experiments. The validation experiment consisted of three different replicates that were compared against model predictions for C_{OG} and *DO* under the action of the low-frequency control strategy. In this case, the predictions followed the trajectory of a single element of fluid travelling through the tube, starting with similar initial conditions and *PID* parameters (Fig. 8).

Before beginning the validation experiments, the model was adjusted to the experimental setting. The gas holdup was measured in the scale-down setting, and the value was inserted into the model, as well as the value of the glucose concentration in the feed solution. Furthermore, the control system input and outputs were adjusted to match the ones of our control software. For this, the manipulated variable F_{FEED} was converted to the percentage of the maximum pump flowrate by using a calibration curve of the feed pump. Furthermore, the control variable C_{OG} was converted to % v/v. These new variables were used for designing the control system to be implemented in the lab-scale photobioreactor. The residence time (i.e. the time between two distinct control actions) was set to 700 s both in the model and in the experimental control system with the purpose of mimicking the pilot-scale photobioreactor. Finally, the results from the model, the concentration profiles in the length of the tube and time, were converted into the profiles in time from the point of view of the fluid travelling through the tube. This allowed us to compare the modelling results with the experimental data from the photobioreactor runs.

These runs were executed consecutively and were named as replicate 1, 2 and 3 following their chronological order. For the sake of technical

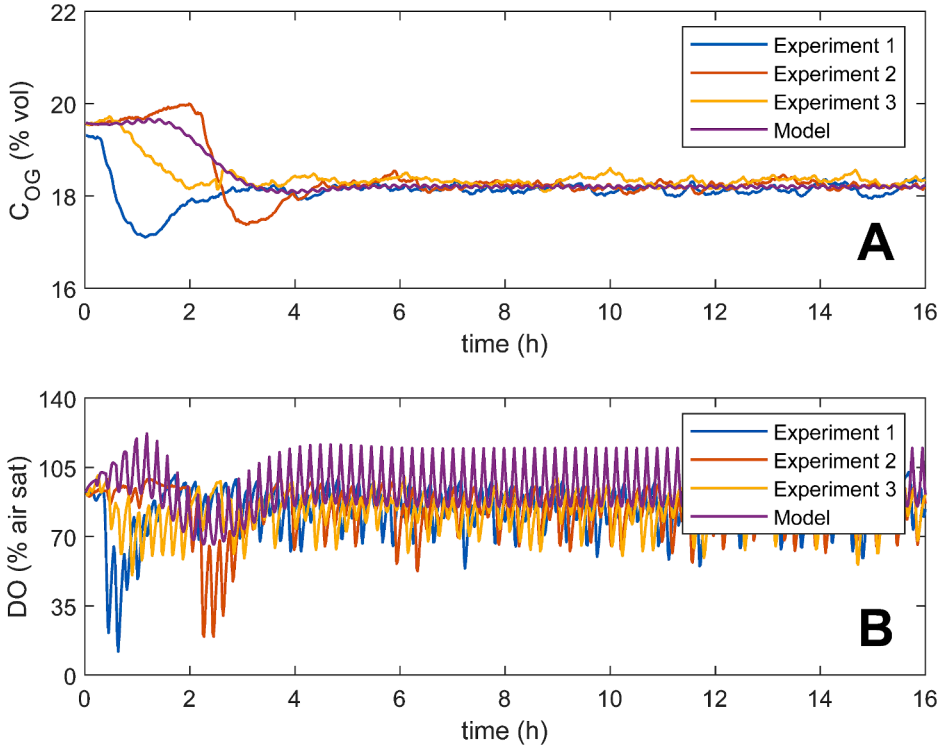

Fig. 8. Validation experiment and control results for C_{OG} (A) and *DO* (B). Experiment 1 is depicted in blue, experiment 2 in orange, Experiment 3 in yellow and model predictions in purple. (For interpretation of the references to colour in this figure legend, the reader is referred to the web version of this article.)

simplicity, the validation experiment was carried out with a constant light input. The C_{OG} setpoint in the experiments was set to 17 % v/v, which after adjusting for the 10 mbar water lock overpressure results in a real value of 18 % v/v. On the other hand, the simulation *in silico* was run with a setpoint of 18.2 % v/v. The reason for this difference is that the pressure of the water lock was not adjusted depending on the atmospheric pressure changes. Because of that, the real setpoint concentrations in the validation experiments were 18.1, 18.2 and 18.3 % v/v for replicate 1, 2 and 3, respectively. Accordingly, we selected 18.2 % v/v to run the comparison simulations in the model as it is the average of the three values. We considered that this fact did not affect significantly affect the conclusions from the comparison.

C_{OG} reached a stable value, that is, oscillating within a range of ± 2 % from the setpoint, 1.8, 3.7 and 2.0 h after the start of replicates 1, 2 and 3, in that order (Fig. 8A). The response of the controller in the validation was faster for replicate 1 and 3 than in the case of the model. The model predicted reaching stability after 3.5 h, similarly to replicate 2. Moreover, the evolution of C_{OG} in the reactor followed a similar pattern as in the computational simulation, although with less accused dynamics. First, there was a slight concentration increase from the initial equilibrium with air that was followed by a drop before C_{OG} stabilized. While in replicate 2 this drop in C_{OG} occurred around the same time as in the model, in replicate 1 it was deeper and happened considerably before, already within the first hour. In addition, replicate 3 showed a less pronounced drop, equivalent to the prediction, but occurred an hour before. Similar dynamics were also observed in the *DO* profiles obtained in the model and during the experiment (Fig. 8B). Stability was reached after an initial drop in *DO*, that was deeper in replicates 1 and 2 and occurred earlier than the prediction in replicates 1 and 3.

The reason behind the pronounced and early drop in experiment 1 lies in the initial real C_{OG} setpoint that was used at the beginning of the experiment, 21 % v/v. Because this concentration was above the initial concentration in the reactor, the controller was inactive during the first 20 min of the run and no glucose was being added. As a consequence, photosynthesis became limited by CO_2 very fast and no O_2 was produced. At that point, we manually provided a glucose pulse as a kick-off for the mixotrophic metabolism, causing the observed early decrease in C_{OG} and the activation of the controller. On top of that, we also decreased the setpoint to 18 %, which was maintained that way for the rest of the experiment. While the manual pulse and the setpoint change partially affected the dynamics of the system, the amount of glucose supplied to the *STR* was similar in the three replicates, being an average of 2.5 ± 0.4 g L^{-1} day^{-1} of glucose. Furthermore, this value is close to the 1.8 g L^{-1} day^{-1} of glucose predicted by the model for equivalent conditions.

Interestingly, the oscillations obtained after reaching stability were slightly stronger in the experiments and *DO* decreased to lower concentrations than in the computational simulation. While the reasons for this behaviour remain obscure, a possible explanation might come from the higher amount of glucose provided in the validation experiment. In addition, the quick and deep response in the validation experiments suggests that the q_{smax} that we had determined in the *BOM* underestimated its real value (Appendix 2). Small variations in the physiological state of the cultures [25] and the linearization bias [26] may introduce sources of inaccuracies, making the estimation of Monod parameters nontrivial. In addition, deviations in the determination of $k_{OL}a$ in the *TPBR* and the extrapolation to our scale-down setup could have also played a role. Moreover, we cannot exclude the possibility that different degrees of biomass adaptation happened during the continuous experiment, contributing to the divergence in experimental results. We have previously observed that glucose metabolism can influence pigment content in *G. sulphuraria* [12,13]. In light of this, the employed empirical $q_{O,auto}$ could have been overestimated as it was measured in an autotrophic culture. Regardless, achieving an extremely high level of precision was not the primary objective of this model; instead, its purpose was to serve as a practical tool for facilitating the scale-up process.

Overall, we can conclude that the model compared to the empirical results reasonably well. The controller designed *in silico* can be used as the starting point for the scale-up of the process. Even so, the model can still be improved to match more accurately the results obtained in the lab. Further insight into the kinetic parameters of the strain used is a good point to start. In addition, the scale-down approach was successful but the experimental design can still be improved to simulate more complex conditions, such as dynamic light.

4. Conclusions

This study presents a comprehensive approach for modelling and controlling the kinetics of oxygen-balanced mixotrophy (*OBM*) in a tubular photobioreactor using the tank-in-series approach and proportional-integral-derivative (*PID*) controllers. The optimal representation of our reference pilot-scale reactor was achieved with a configuration of 100 stages, offering the ideal balance between accuracy and computational burden. Model simulations revealed a downward trend over time in dissolved oxygen (*DO*) and oxygen concentration in the gas phase (C_{OG}) in the simplified scenario with constant light input and balanced glucose supply. This trend is attributed to the faster rate of heterotrophic metabolism and the presence of a bleed gas flowrate due to the accumulation of CO_2 in the gas phase.

PI and *PID* controllers were designed and compared relying on the ultimate gain method with constant light and a controller with low-frequency error definition. The *PID* controller resulted in the best performance and was implemented with real outdoor conditions with two error definitions: low-frequency and high-frequency. The high-frequency strategy underwent trial and error fine-tuning before implementation. Both strategies effectively maintained stable C_{OG} with oscillations between 16 and 24 % v/v and ensured *DO* levels stayed in the range of 10 to 180 % air saturation when subjected to clear sky and cloudy weather. The high-frequency strategy exhibited reduced glucose accumulation while supplying a marginally smaller amount.

The validation experiments corroborated model predictions for C_{OG} and *DO*. Yet, the dynamics observed in the experiments for C_{OG} and *DO* were faster and steeper, a disparity that may be attributed to the accuracy measuring Monod kinetic parameters. However, a stable state was always reached between 1.8 and 3.7 h, comparable with the 3.5 h predicted by the model. The overall success of the proposed methodology highlights its viability over conventional trial-and-error approaches, particularly in the context of *OBM* scale-up and large-scale bioprocess control.

Funding

This work was supported by ProFuture project (2019–2023) "Microalgae protein-rich ingredients for the food and feed of the future"-H2020 Ref. 862980.

CRediT authorship contribution statement

Pedro Moñino Fernández: Writing – review & editing, Writing – original draft, Visualization, Methodology, Investigation, Formal analysis, Data curation, Conceptualization. **Luca Buscaglia:** Writing – review & editing, Visualization, Methodology, Investigation, Formal analysis, Data curation, Conceptualization. **Daan Jordaan:** Investigation, Formal analysis. **Maria Barbosa:** Writing – review & editing, Supervision, Funding acquisition. **Marcel Janssen:** Writing – review & editing, Supervision, Conceptualization.

Declaration of competing interest

The authors declare that they have no known competing financial interests or personal relationships that could have appeared to influence the work reported in this paper.

Data availability

Data will be made available on request.

Acknowledgements

The authors thank Renske Rinzema and Fernando Zetrialdi for their contribution in the tracer experiment and the mass transfer coefficient determination.

Appendix A. Supplementary data

Supplementary data to this article can be found online at https://doi.org/10.1016/j.cej.2024.155718.

References

[1] A. Aguilar, T. Twardowski, R. Wohlgemuth, Bioeconomy for sustainable development, Biotechnol. J. 14 (8) (2019) 1800638, https://doi.org/10.1002/biot.201800638.
[2] Y. Lokko, M. Heijde, K. Schebesta, P. Scholtès, M. Van Montagu, M. Giacca, Biotechnology and the bioeconomy—Towards inclusive and sustainable industrial development, New Biotechnol. 40 (Jan. 2018) 5–10, https://doi.org/10.1016/j.nbt.2017.06.005.
[3] S.-O. Enfors, et al., Physiological responses to mixing in large scale bioreactors, J. Biotechnol. 85 (2) (Feb. 2001) 175–185, https://doi.org/10.1016/S0168-1656(00)00365-5.
[4] A.R. Lara, E. Galindo, O.T. Ramírez, L.A. Palomares, Living with heterogeneities in bioreactors, Mol. Biotechnol. 34 (3) (Nov. 2006) 355–381, https://doi.org/10.1385/MB:34:3:355.
[5] G. Wang, C. Haringa, H. Noorman, J. Chu, Y. Zhuang, Developing a computational framework to advance bioprocess scale-up, Trends Biotechnol. 38 (8) (Aug. 2020) 846–856, https://doi.org/10.1016/j.tibtech.2020.01.009.
[6] M.J. Barbosa, M. Janssen, C. Südfeld, S. D'Adamo, R.H. Wijffels, Hypes, hopes, and the way forward for microalgal biotechnology, Trends Biotechnol. 41 (3) (Mar. 2023) 452–471, https://doi.org/10.1016/j.tibtech.2022.12.017.
[7] O. Bernard, F. Mairet, and B. Chachuat, "Modelling of Microalgae Culture Systems with Applications to Control and Optimization," in *Microalgae Biotechnology*, C. Posten and S. Feng Chen, Eds., in Advances in Biochemical Engineering/Biotechnology. , Cham: Springer International Publishing, 2016, pp. 59–87. doi: 10.1007/10_2014_287.
[8] I. Fernández, M. Berenguel, J.L. Guzmán, F.G. Acién, G.A. De Andrade, D. J. Pagano, Hierarchical control for microalgae biomass production in photobiorreactors, Control Eng. Pract. 54 (Sep. 2016) 246–255, https://doi.org/10.1016/j.conengprac.2016.06.007.
[9] A. Pawłowski, J. L. Guzmán, M. Berenguel, F. G. Acíen, and S. Dormido, "Application of Predictive Feedforward Compensator to Microalgae Production in a Raceway Reactor: A Simulation Study," *Energies*, vol. 11, no. 1, Art. no. 1, Jan. 2018, doi: 10.3390/en11010123.
[10] E. Rodríguez-Miranda, M. Beschi, J. L. Guzmán, M. Berenguel, and A. Visioli, "Daytime/Nighttime Event-Based PI Control for the pH of a Microalgae Raceway Reactor," *Processes*, vol. 7, no. 5, Art. no. 5, May 2019, doi: 10.3390/pr7050247.
[11] S. Tebbani, F. Lopes, and G. Becerra Celis, "Nonlinear control of continuous cultures of Porphyridium purpureum in a photobioreactor," *Chem. Eng. Sci.*, vol. 123, pp. 207–219, Feb. 2015, doi: 10.1016/j.ces.2014.11.016.
[12] F. Abiusi, E. Trompetter, H. Hoenink, R.H. Wijffels, M. Janssen, Autotrophic and mixotrophic biomass production of the acidophilic Galdieria sulphuraria ACUF 64, Algal Res. 60 (Dec. 2021) 102513, https://doi.org/10.1016/j.algal.2021.102513.
[13] F. Abiusi, P. Moñino Fernández, S. Canziani, M. Janssen, R. H. Wijffels, and M. Barbosa, "Mixotrophic cultivation of Galdieria sulphuraria for C-phycocyanin and protein production," *Algal Res.*, vol. 61, p. 102603, Jan. 2022, doi: 10.1016/j.algal.2021.102603.
[14] F. Abiusi, R.H. Wijffels, M. Janssen, Doubling of microalgae productivity by oxygen balanced mixotrophy, ACS Sustain. Chem. Eng. 8 (15) (Apr. 2020) 6065–6074, https://doi.org/10.1021/acssuschemeng.0c00990.
[15] F. G. Acién Fernández, J. M. Fernández Sevilla, J. A. Sánchez Pérez, E. Molina Grima, and Y. Chisti, "Airlift-driven external-loop tubular photobioreactors for outdoor production of microalgae: assessment of design and performance," *Chem. Eng. Sci.*, vol. 56, no. 8, pp. 2721–2732, Apr. 2001, doi: 10.1016/S0009-2509(00)00521-2.
[16] P. Moñino Fernández, A. Vidal García, T. Jansen, W. Evers, M. Barbosa, and M. Janssen, "Scale-down of oxygen and glucose fluctuations in a tubular photobioreactor operated under oxygen-balanced mixotrophy," *Biotechnol. Bioeng.*, vol. 120, no. 6, pp. 1569–1583, 2023, doi: 10.1002/bit.28372.
[17] O. Levenspiel, "The Tanks-in-Series Model," in *Tracer Technology: Modeling the Flow of Fluids*, O. Levenspiel, Ed., in Fluid Mechanics and Its Applications. , New York, NY: Springer, 2012, pp. 81–97. doi: 10.1007/978-1-4419-8074-8_8.
[18] A.M.J. Kliphuis, A.J. Klok, D.E. Martens, P.P. Lamers, M. Janssen, R.H. Wijffels, Metabolic modeling of Chlamydomonas reinhardtii: energy requirements for photoautotrophic growth and maintenance, J. Appl. Phycol. 24 (2) (Apr. 2012) 253–266, https://doi.org/10.1007/s10811-011-9674-3.
[19] J.G. Ziegler, N.B. Nichols, Optimum settings for automatic controllers, Trans. Am. Soc. Mech. Eng. 64 (8) (1942) 759–765, https://doi.org/10.1115/1.4019264.
[20] B. Ogunnaike and W. H. Ray, *Process Dynamics, Modeling, and Control*. in Topics in Chemical Engineering. Oxford, New York: Oxford University Press, 1995.
[21] R. Lau, W. Peng, L.G. Velazquez-Vargas, G.Q. Yang, L.-S. Fan, Gas−liquid mass transfer in high-pressure bubble columns, Ind. Eng. Chem. Res. 43 (5) (Mar. 2004) 1302–1311, https://doi.org/10.1021/ie030416w.
[22] R. Sander, Compilation of Henry's law constants (version 4.0) for water as solvent, Atmospheric Chem. Phys. 15 (8) (Apr. 2015) 4399–4981, https://doi.org/10.5194/acp-15-4399-2015.
[23] F. Abiusi, R.H. Wijffels, M. Janssen, Oxygen balanced mixotrophy under day-night cycles, ACS Sustain. Chem. Eng. 8 (31) (Aug. 2020) 11682–11691, https://doi.org/10.1021/acssuschemeng.0c03216.
[24] J. A. Baeza, "18 - Principles of Bioprocess Control," in *Current Developments in Biotechnology and Bioengineering*, C. Larroche, M. Á. Sanromán, G. Du, and A. Pandey, Eds., Elsevier, 2017, pp. 527–561. doi: 10.1016/B978-0-444-63663-8.00018-5.
[25] K. Kovárová-Kovar, T. Egli, Growth kinetics of suspended microbial cells: from single-substrate-controlled growth to mixed-substrate kinetics, Microbiol. Mol. Biol. Rev. 62 (3) (Sep. 1998) 646–666.
[26] L.H. Smith, P.L. McCarty, P.K. Kitanidis, Spreadsheet method for evaluation of biochemical reaction rate coefficients and their uncertainties by weighted nonlinear least-squares analysis of the integrated monod equation, Appl. Environ. Microbiol. 64 (6) (Jun. 1998) 2044–2050, https://doi.org/10.1128/AEM.64.6.2044-2050.1998.